Surface & Coatings Technology 402 (2020) 126502

Contents lists available at ScienceDirect

Surface & Coatings Technology

journal homepage: www.elsevier.com/locate/surfcoat

The role of microstructure and cathodic intermetallics in localised deposition mechanism of conversion compounds on Al (Si, Fe, Cu) alloy

Salil Sainis[a,*], Sabrina Roșoiu[b], Ehsan Ghassemali[a], Caterina Zanella[a]

[a] Department of Materials and Manufacturing, School of Engineering, Jönköping University, Gjuterigatan 5, Jönköping 55111, Sweden
[b] Centre for Surface Science and Nanotechnology, University Politehnica of Bucharest, Splaiul Independentei 313, 060042 Bucharest, Romania

ARTICLE INFO

Keywords:
Cerium
Conversion coatings
Al-Si cast
SEM
AFM
SKPFM
Microstructure-induced localised deposition

ABSTRACT

Cerium-based conversion coating formation is triggered by a local rise in pH at cathodic sites produced by the oxygen reduction reaction. Therefore, size, morphology distribution and electrochemical potential of those sites play a crucial role. While the deposition reaction is sensitive to both immersion bath concentrations and underlying substrate microstructure, only the former has been widely investigated. This research attempts to fill the gap by studying the effect of controlled microstructure variables like the cathodic intermetallics' geometry and spatial distribution on the conversion compound deposit initiation. A controlled cast Al alloy was synthesised for this study and consisted of distinct cathodic phases: Cu-rich intermetallics, Fe-rich intermetallics and Si particles. The localised deposition preferentially formed only on strong cathodic Cu-rich intermetallics. Size (surface area) of the Cu-rich intermetallic correlated linearly with the deposited area over it in terms of lateral and z-direction spread. The pH gradient occurring from the oxygen reduction near an IM is very local and does not affect pH gradients of a neighbouring IM. When immersion time is increased from 0.5 h to 1 h, the percentage of Cu-rich IM covered with conversion coating increases. Big Cu-rich IM activate faster for deposition reaction than small Cu-rich IM.

1. Introduction

Localised corrosion damage in aluminium alloys occurs due to heterogeneities in the microstructure. Second phases or intermetallic (IM) particles, especially those containing Cu and Fe, show cathodic behaviour compared to anodic aluminium matrix [1–3] and form a local micro-galvanic couple leading to corrosion damage [4–7]. Systems for corrosion protection consist typically of multi-layered coatings, the first layer of which is often a conversion coating [8]. The conversion layer is composed of compounds that are more stable than native oxides in aggressive environments and thus providing corrosion protection.

Several conversion coating treatments, like those based on cerium as reviewed by Harvey [9], trivalent chromium as reviewed by Mitton et al. [10] and Ti-Zr [11–15], form the protective layer with the same underlying mechanism. The conversion coating deposition mechanism leverages the electrochemical corrosion reaction from the galvanic coupling between microstructural second-phases and aluminium matrix to form precipitates that in-turn block the corrosion reaction. On the cathodic sites of the microstructure, a local rise in pH [16–18] occurs due to the formation of OH^- ions from the cathodic reduction of oxygen. Local hydroxide anions in vicinity of cathodic sites combine with respective cations from solution to form a local deposit. Such local-pH-increase-driven-deposition reactions have been observed on aluminium alloys by immersion in conversion coating treatments based on cerium [18–32], Ti-Zr [15,33–41] and trivalent chromium [35,42–46]. Among the several types of pre-treatment layers forming by this deposition mechanism, cerium-based conversion coating (CeCC) is the most investigated. The offered corrosion inhibition in CeCC is attributed to physical barrier formation by insoluble precipitates of cerium oxides and hydroxides [47] over cathodic sites. Blocking of the localised microstructural cathodic activity [21] and consequently, the associated anodic reaction related to the micro-galvanic coupling leads to a decrease in i_{corr} [19], ultimately causing increased corrosion resistance. Due to the extensive literature available, this study will employ CeCC to investigate the localised-ph-increase-driven deposition mechanism further.

The spontaneous coating deposition reactions upon immersion of the substrate in cerium ion-containing solution are described in the literature to be multi-step – 'island initiation' at cathodic sites and 'coalescence' to further cover the entire surface [18]. The factors influencing deposition include the immersion bath process parameters (pre-treatments, concentration of immersion solution, type of salt in solution, pH, time of immersion, temperature of bath and use of additives) reviewed

* Corresponding author at: Department of Materials and Manufacturing, School of Engineering, Jönköping University, Gjuterigatan 5, P.O. Box 1026, SE-551 11 Jönköping, Sweden.
E-mail address: Salil.sanis@ju.se (S. Sainis).

https://doi.org/10.1016/j.surfcoat.2020.126502
Received 9 July 2020; Received in revised form 6 October 2020; Accepted 10 October 2020
Available online 17 October 2020
0257-8972/

extensively by Harvey [9], and the underlying microstructure of the aluminium alloy substrate. Spontaneous deposition of conversion coatings by immersion in a cerium ion containing solution is kinetically slow, and to accelerate the process oxidants like H_2O_2 [31,48–59], $NaClO_4$ [51–53,60] and $KMnO_4$ [60–62] have been used promote more rapid deposition. H_2O_2 is the most common additive in cerium conversion coating solutions, being an oxidant it provides additional hydroxide ions and promotes the precipitation reaction [59].

The microstructure of alloy substrates, especially the cathodic IM particles, plays a crucial role on the precipitate 'island initiation', a phenomenon central to CeCC deposition mechanism. Local precipitates of CeCC have been observed to form on cathodic IM Al_7Cu_2 [22], S-phase Al_6(Cu, Fe, Mn) [26,63] of AA2024, Al_6-(Mn, Fe-Cr) [24] of AA5083, Fe-rich IM Al-Si cast alloys [32]. The study by Hughes et al. [20] has demonstrated that Al-Cu IM have a much thicker coating compared to that over Mn-Fe IM. They established that the rate of oxygen reduction is a function of electrochemical activity of IM and that more active IMs show higher precipitation compared to other IMs with lesser cathodic activity. Furthermore, in the same study, the extent of deposition was observed to be a function of cathodic particle size. The precipitate thickness was observed to be higher on larger IM like Al_2Cu_2Fe and $AlCu(Mn,Fe)_3$ in comparison to smaller cathodic particles such as dispersoid and hardening precipitates.

Several researchers have reported localised deposition on other cathodic IM sites [22,24–26,28,63,64]. Because the IM particles are significantly affecting the initiation of precipitation product under their effect on the rise of local pH at cathodic sites, their electrochemical and geometrical properties critically influence the conversion layer. Microstructure, or more specifically the cathodic IM particles, has not been a variable in explaining the deposition mechanism as most studies use commercial alloys like AA2024 and AA7075 where the microstructure is fixed by the standard composition and processing route. This research attempts to cover the gap by controlling the microstructure and study its effect on the CeCC nucleation and growth as a function of (1) IM size (2) IM spatial distribution (3) IM neighbourhood.

For such an investigation, a relatively simple microstructure has been tailored to contain different nobility phases rich in Cu, Fe and Si respectively. The model alloy was subjected to directional solidification at two starkly different cooling rates to obtain two types of microstructure where these three cathodic phases have the same composition but have very different size and spatial distribution. The surface activation treatments, immersion bath concentrations and IM phase composition have been kept the same, only variables being IM size and their spatial distribution. Details of the precipitation initiation and evolution sequence have been investigated by performing quantitative analysis of deposit formation between immersion periods of 0.5 h and 2 h over different IM geometries. Quantitative measurements of deposit were done on microstructural observations obtained using Scanning Electron Microscopy (SEM) and Atomic Force Microscopy (AFM). Scanning Kelvin Probe Force Microscopy (SKPM) was used to characterise the volta potential of the different IMs. Finally, cathodic potentiodynamic polarization has been performed on the pre-coated and conversion coated samples to determine if the localised deposits help in inhibiting the cathodic current.

2. Materials and methods

2.1. Materials

Table 1 shows the chemical composition of model cast Al-Si alloys used in this study. Pure aluminium (99.9% purity with 0.1 wt% Fe impurity) along with alloying element Cu and Fe were melted in a Nabtherm Tilting Furnace at 800 °C and cast in cylindrical graphite moulds. The cast samples were re-melted at 710 °C and then subjected to solidification at different pulling rates (0.03 mm/s and 6 mm/s) in a Bridgeman furnace to obtain "coarse" and "fine" microstructure, respectively.

Table 1
Selected composition for the model alloy.

Element	Al	Si	Cu	Fe
wt.%	Balance	7.0	2.0	1.0

2.2. Methods

2.2.1. Sample preparation

The directionally solidified cylindrical rods were cut in cross sectional direction (discs of ⌀10 mm × 10 mm) and mounted in a non-conductive epoxy resin of size ⌀30 mm × 20 mm. The samples embedded in the epoxy resin were ground with papers of grit size P320, P800, P1000, P2000, P4000 and then polished with a diamond suspension of colloidal particle size 3 μm, 1 μm and 0.1 μm. They were then rinsed in acetone ultrasonic bath for 15 min to remove the residues of polishing and to degrease the surface.

2.2.2. Surface preparation before coating treatment

The native aluminium oxide layer was removed by etching the polished aluminium alloy surface with a 0.05 M NaOH solution for 2 min followed by acid pickling in 1:1 HNO_3 solution for 30 s. Between the steps of etching and pickling and after the final pickling step, the surface was thoroughly rinsed with distilled water to remove any loosely bound products of the dissolution reaction. A water film was maintained at all times after each to prevent exposure of etched and pickled surfaces with air.

2.2.3. Coating deposition

Samples were then immediately immersed in a freshly prepared conversion coating treatment bath of composition 0.1 M $Ce(NO_3)_3$ + 0.1 M NaCl (pH 2.8) at room temperature and immersed for three different times 0.5 h, 1 h and 2 h. Immersion was carried out in a cylindrical container of diameter 9 mm filled with 250 mL coating solution. Each conversion coating treatment was performed twice on two different specimens. After the respective immersion times, the samples were removed from the bath and rinsed with distilled water. Cleaned samples after deposition were placed in a desiccator for thorough drying before being taken for various characterisations.

Each conversion coating treatment was performed twice on two different specimens.

2.3. Surface characterisation

Microstructure and surface morphology of bare and conversion coating deposited samples were characterised using JOEL JSM-7001F SEM in the secondary electron imaging mode at an accelerating voltage of 5 kV. The characterisation of "before" and "after" deposition morphology for each immersion time on the slow and fast solidification rate samples was repeated twice on specimens from two different cylindrical rods.

Additionally, the phases of the samples were investigated by Rigaku SmartLab X-ray Diffractometer (XRD) system (with a Cu K_α radiation, λ = 1.5405 Å), operating at room temperature within the 2theta range 5°–90°.

Surface topography of local deposits was performed using a Park Systems NX10 AFM in non-contact mode. The local electrochemical properties of the different intermetallics were characterised using SKPM.

Cerium conversion coatings reduce corrosion by inhibiting the cathodic reaction. To study the efficiency of cathodic inhibition after localised conversion coating depositions, the samples were polarized only at cathodic potentials sweeping at 0.16 V/s scan rate in a 0.05 M NaCl solution and the current was measured using a potentiostat. The potentiodynamic polarization was started 600 s after immersion in 0.05 M NaCl solution. The reference electrode used in the study was an Ag/AgCl 3 M KCl electrode (+0.220 V *vs* SHE) and a platinum counter electrode was used.

2.4. Image analyses

For the image analysis, for each experimental condition, eight different regions were investigated from two specimens before and after deposition. The quantifications of uncovered IM and deposited features of the microstructures were carried out using image analysis software ImageJ [65]. In coarse microstructure, each region investigated has dimensions 32 × 43 μm while each region in fine microstructure investigated had a dimension of 4 × 5 μm. The IM boundary was sketched by 'Freehand selection' tool of ImageJ and its area measured by the same software. 'Nearest neighbour distance' reported in this study was measured as the distance between a point on the circumference of a Cu-rich IM and the circumference of its nearest Cu-rich IM.

3. Results and discussion

3.1. Characterisation of tailored cast Al alloy microstructure

Cast Al-Si alloys solidify with a microstructure consisting of α-aluminium dendrites and the inter-dendritic regions contain aluminium-silicon eutectic [66]. Phosphorus is a common impurity existing in trace amounts in aluminium alloys, and its compound AlP acts as a nucleating site for IM [67]. IM nucleate and grow in the eutectic Al-Si regions between the primary aluminium dendrites. The spacing between the arms of the dendrites – Secondary Dendritic Arm Spacing (SDAS) is a function of the solidification rate. The average value of SDAS for slow and fast solidified alloy were 76.5 ± 8.7 μm and 10.2 ± 1.1 μm, respectively. Slow and fast solidified microstructures are hereafter referred to as 'coarse' and 'fine' respectively. The microstructure containing either (a) big and sparsely spaced IM or (b) small and closely spaced IM can thus be tailored by changing the rate at which solidification takes place (Fig. 1(a) and (b), respectively).

Different types of IMs formed in both coarse and fine microstructure (Fig. 1(a) and (b)) are (1)β-Al_5FeSi (2)θ-Al_2Cu (3) ω-Al_7Cu_2Fe. The β IMs, in both slow and fast solidification microstructures, show a needle-shaped morphology [68,69]. Cu-containing IMs θ and ω have a more "rounded morphology". Because IM cannot always be identified accurately by their morphology [70], they have been additionally characterised using EDX and XRD. Fig. 1(c) and (d) shows the corresponding elemental maps of microstructures. The average atomic fraction of different elements in the two types of intermetallics β and θ characterised using EDX point analysis is presented in Table 2. The proportion of elements obtained using EDX point analysis does not match exactly with the stoichiometry of the intermetallic compounds, as the EDX beam has a certain volume interaction that may exceed the volume of the intermetallic, especially so in the fine microstructure with small intermetallics. Furthermore, XRD technique was used to confirm the presence of the different IM phases (Fig. 2) Al [71], Si [72], β-Al_5FeSi [68,73–75], θ-Al_2Cu [73,76–78] and ω-Al_7Cu_2Fe [77,78].

The coarse microstructure's IM phases of plate-like β, rounded θ and ω IM were measured to be in the range 20–100 μm long and 2–10 μm wide, 2–20 μm in equivalent diameter and 0.1–1 μm width respectively. On the other hand, the dimensions of plate-like β, rounded θ and ω in the fine microstructures were in the range 1–20 μm in length and 0.1–1 μm in width, 1–8 μm in equivalent diameter and 0.1–1 μm in diameter, respectively. The average nearest neighbour distance for coarse and fine microstructure was 49.0 ± 6.8 μm and 8.0 ± 0.9 μm respectively.

The relative nobility of the different phases were characterised by mapping the relative volta potential of the microstructure using SKPM (Fig. 3(a)). Volta potential profile in Fig. 3(b) of the line segment in Fig. 3(a) shows that the two compositionally different Cu-containing IM θ and ω have higher volta potential than Al and β. While the ω (Al,-Cu,Fe) has slightly lower volta potential than θ(Al,Cu), they are both treated as "Cu-rich" from hereon. Fe-containing IM β have relatively higher volta higher than Al, but lower than that of Cu-rich IM indicating that they are weakly cathodic. They are referred to as "Fe-rich" IM from hereon. Si particles had similar SKPM potential as Cu-rich IM (Fig. 3(b)).

3.2. Characterisation of cerium conversion compounds deposits

All substrates were subjected to the same surface preparation methods elucidated in the experimental section and then immersed in a solution of 0.1 M $Ce(NO_3)_3$ + 0.1 M NaCl for three different times 0.5 h, 1 h and 2 h. The "before" and "after" deposition for numerous substrates in two different IM sized microstructure were characterised with secondary electron imaging mode of an SEM. An exemplar is shown in Figs. 4 and 5, respectively, for coarse and fine IM. The local deposits on cathodic sites had a "cracked mud" like morphology, which has also been observed in other studies [21,27,31,79,80]. The depositions were observed to occur preferentially on Cu-rich IM θ and ω but were not evident on the plate-like β (hereby referred to as "Fe-rich") unless they were attached to the Cu-rich IM, in which case the deposit extended over the Fe-rich IM covering it partially. IM β is weakly cathodic, and so the oxygen reduction reaction did not yield a sufficiently high concentration of OH^- ions needed for the precipitation of conversion compounds. Hughes et al. [20] have reported differences in the extent of deposition due to different cathodic reduction efficiencies of different composition IM. Si particles did not show any deposition unless they were in attached to Cu-containing IM in which case the deposit extended over the Si particle covering it partially. Even though volta potential maps in Fig. 3 showed that Si particles and Cu-containing IM have nobilities, the localised precipitating reaction did not occur on Si particles.

Cerium conversion deposits have been observed on Si particles and weakly cathodic Fe-rich IM in the study by Eslami et al. [31] in a non-copper-containing alloy immersed in the same solution for 18 h. The mechanism proposed by them professes that heavier deposition becomes possible only when Al from β-Al_5FeSi selectively dissolves, enriching the IM with Fe and Si, making it more cathodic to support precipitation of conversion compounds. No deposit were observed on Fe-rich β or on Si particles after 18 h immersion on the alloy used in the current study with the same solution as used by Eslami et al. [25]. In Cu-rich phase containing microstructure, the very active IM sites preferentially deposit conversion compounds on them, and a thin conversion layer is formed on the rest of the alloy surface. The activity of weakly cathodic Fe-rich β phase and Si particles is diminished due to the formation of a thin passive layer on them and even long immersion times of 18 h show no precipitate build-up.

Increased pH region extending beyond the IM boundary has been reported before in a study by Hughes et al. [18] to be ~20% more than the total size of the Cu-rich IM for short immersion times up to 4 min. In the current study, the area of local deposit forming on coarse Cu-rich IM was on average, 316 ± 96%, 192 ± 25% and 234 ± 44% of the area of IM respectively for immersion times 0.5 h, 1 h and 2 h. On fine Cu-rich IM, the deposit was on average, 301 ± 42%, 313 ± 50% and 241 ± 27% of the area of IM respectively for immersion times 0.5 h, 1 h and 2 h. The margin of error reported here is at 95% confidence level.

IM particle size and spacing influence the corrosion kinetics of alloys [81,82]. Because the conversion coating deposition reaction leverages the IM-Al matrix micro-galvanic corrosion reaction for deposition of conversion compounds, the IM spatial distribution and size can also influence the conversion coating deposition reaction. These microstructural factors are quantitatively analysed and discussed below.

3.2.1. Influence of IM neighbourhood and spatial distribution on the deposition reaction

The Cu-rich IM exist in different neighbourhoods, all present in an aluminium matrix. They are classified as (●) independently existing, (♦) attached to a β IM plate, (▲) attached to Si particle, (■) attached to both Si and β (Fig. 4(a), (b) and (c)). The different neighbourhoods demonstrate different scenarios of micro-galvanic coupling. Deposition on independent IM spread equally in all directions across the Cu-rich IM/Al

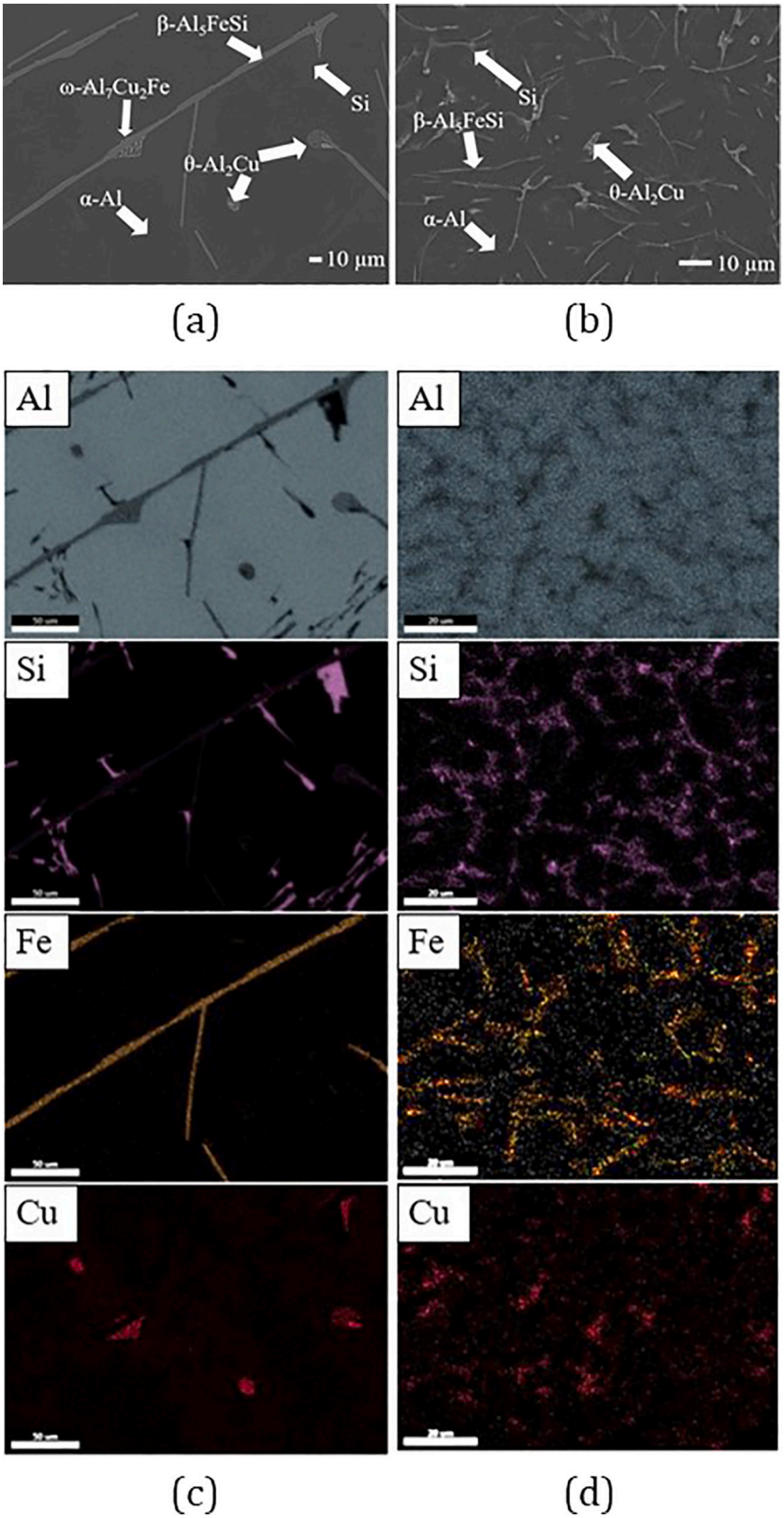

Fig. 1. Cast alloy Al-7Si-2Cu-1Fe characterised with SEM in secondary electron imaging mode to show differences in microstructure when slow and fast solidified respectively: (a) big IM that are spaced father apart with greater average nearest neighbour distance (b) small IM that are closer together with lesser nearest neighbour distance (c) elemental map of microstructure in Fig. 1(a) obtained using EDX at accelerating voltage 20 kV and (d) elemental map of microstructure in (b).

Table 2
EDX spot analysis of different intermetallics in coarse and fine microstructure.

Microstructure	Intermetallic	Al (at.%)	Si (at.%)	Fe (at.%)	Cu (at.%)
Coarse	Fe-rich β	66.0 ± 0.8	16.3 ± 0.8	13.4 ± 0.3	0.2 ± 0.0
	Cu-rich θ	71.2 ± 3.0	3.7 ± 1.3	0.4 ± 0.2	19.2 ± 2.1
Fine	Fe-rich β	91.7 ± 2.5	6.8 ± 2.5	0.5 ± 0.2	1.3 ± 0.9
	Cu-rich θ	82.6 ± 2.8	7.7 ± 2.1	1.5 ± 0.8	8.2 ± 2.0

matrix interface. When the Cu-containing IM is attached to a β – greater lateral spread is observed across the Cu-rich IM/Al matrix interface as compared to Cu-rich IM/Si particle or Cu-rich IM/β IM interface. Because Cu-rich IM is more cathodic than Fe-rich β, a higher pH increase on the strong cathodes compared to that on weak cathodes, leading to preferential heavy precipitation on only the Cu-rich IM. The extent of lateral spread across the Cu-rich IM and Al matrix interface was greater than the extent of spread across the Cu-rich IM and Si particle interface. Due to semiconducting properties of Si particles, they do not provide a good conduction path for the electrons. Negligible amount of oxygen may have been reduced in its vicinity and therefore due to lack of OH^- ions the precipitation reaction did not happen to the same extent on the Si-particle/Cu-rich IM as it did across the Cu-rich IM/Al matrix interface.

The influence of IM spatial distribution on the deposition was studied by plotting 'nearest neighbour distance' *vs* % deposit area extension over IM (Fig. 6). 'Nearest neighbour' to a Cu-rich IM in this study is the nearest Cu-rich IM only. Points with colours red, blue and magenta denote measurements done for deposition over IM after immersion for 0.5 h, 1 h and 2 h respectively. While coalescence of precipitate zones was observed when the IM participating in the deposition reaction were very close (~1 μm), the vicinity of neighbour did not cause the deposit region to be extended much more than average. When two coarse IM are very close, the increased pH regions may overlap, but the overlap was not caused due to a bigger-than-average pH gradient. Similarly, deposits on two finer IM (Fig. 5(a) and (d)) was observed to coalesce due to nearest neighbour distance shorter than deposit extension governed by its particle size. At farther nearest neighbour distances, no coalescence was observed. No trend between nearest neighbour distance *vs* % deposit area over IM is observed in either fine or coarse microstructure as shown in Fig. 6. It can be inferred that the OH^- concentration region is very locally situated over its own IM only and that the OH^- concentration gradient over one IM does not affect OH^- concentration over its nearest neighbour. Proximity does not provide a higher driving force for more precipitation.

3.2.2. *Influence of IM size on deposition*

After analysing the deposition over a population of big and small Cu-rich IM in coarse and fine microstructures respectively (Table 3), it is observed that increasing immersion times led to greater number of IM getting activated for deposition (% number of IM covered with conversion compounds) in both coarse and fine microstructures. Furthermore, bigger IM activated faster than smaller IM. After a short immersion of 0.5 h, over 90% of the big Cu-rich is covered compared to just 63% small Cu-rich IM. After 2 h of immersion, 100% of the big Cu-rich IMs showed deposition compared to only 86% of the small Cu-rich IM. This suggests that the size of the particles and microstructure coarseness impact the number of locally activated sites, more that the local deposits grow. Bigger particles get activated in higher number and the time for full coverage becomes shorter.

Fig. 7 plots a localised deposit area over several individual IMs as a function of its own bare surface area. The localised deposit area is observed to linearly increase with the surface area of the underlying IM. The slopes of the linear correlation line (Table 4) for both coarse and fine microstructures are nearly equal for all immersion times indicating that the once conversion coating spontaneously deposits on an active IM, it does not grow significantly between immersion time 0.5 h and 2 h. The conversion coating formation reaction, while driven by micro-galvanic coupling, is also a self-extinguishing process as the deposit formation entirely or partially blocks the cathodic sites and reduces the electrochemical reaction kinetics.

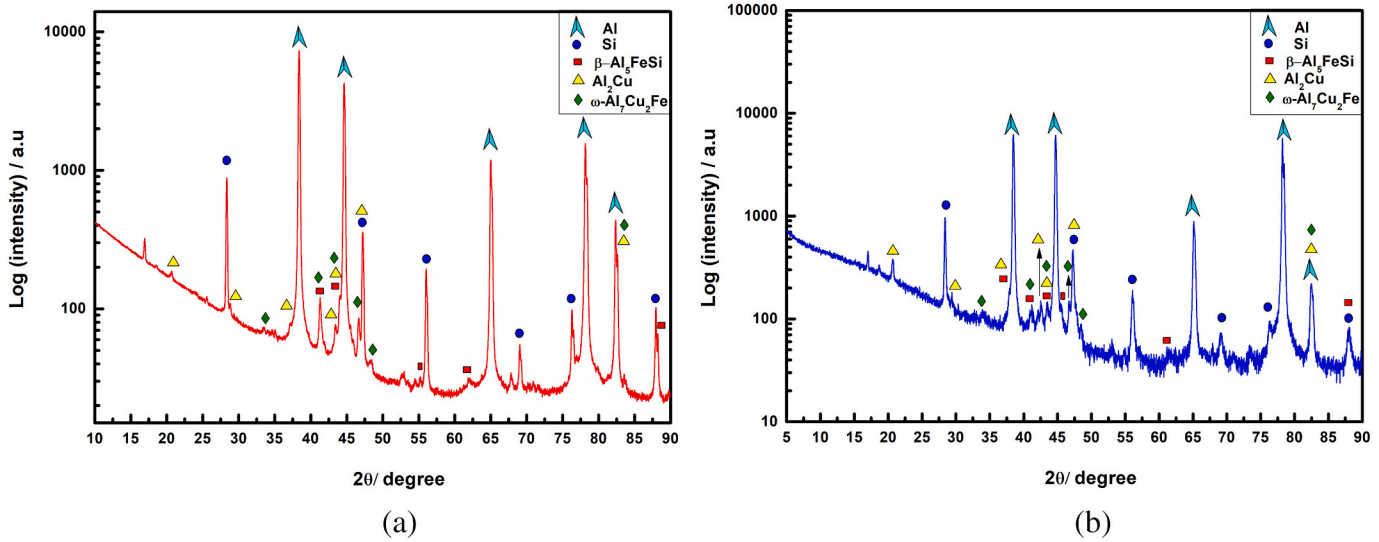

Fig. 2. XRD characterisation for IM validation in alloy Al-7Si-2Cu-1Fe (a) coarse IM (b) fine IM.

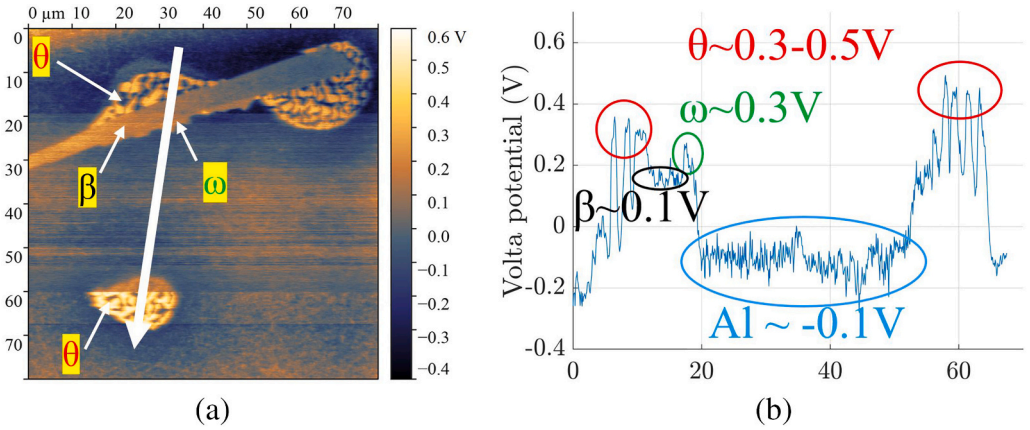

Fig. 3. (a) Volta potential maps of coarse Cu-containing IM θ in different neighbourhoods and (b) corresponding volta potential variation along line segment.

Z-direction topography of deposits over eleven small IMs was characterised using AFM in non-contact mode on the fine microstructure obtained after 2 h immersion. Fig. 8(a) and (b) shows the SEM morphology and AFM topography of the deposited region investigated. Measurements of z-height of deposit over the several IM were found to be between 600 nm and 1600 nm. A strong correlation is found between the IM area and the deposit z-height (Fig. 8(c)). Not only does the precipitation reaction spread radially outward in x- and y-direction but also in the z-direction, all proportional to the IM area.

3.3. Cathodic polarization of samples

CeCC pre-treatments primarily reduce corrosion rate by blocking the cathodic reaction and the samples have been subjected to potentiodynamic polarization only in the cathodic branch. The pre-coated and conversion coated (after 0.5 h, 1 h and 2 h immersion in conversion coating solution respectively) samples were polarized from +0.05 V to −1 V with respect to OCP in a 0.05 M NaCl solution at 0.16 V/s scan rate, and the results are shown in Fig. 9. For each surface treatment condition, the cathodic polarization was performed twice and representative polarization curves are reported. The average cathodic current density ($i_{c,avg.}$) reported in Table 5 is an average value of current density between potential values −100 mV and −400 mV with respect to OCP. E_{corr} is also reported in the table and the value is not influenced by the immersion time in the coating solution. Compared to the $i_{c,avg.}$ of pre-coated surface (etched and pickled), all conversion coated surfaces showed lower $i_{c,avg.}$. The scatter in $i_{c,avg.}$ values obtained from cathodic polarization of 0.5 h, 1 h and 2 h immersion coated samples is high and thus no definitive trend between immersion time and cathodic inhibition effect can be established. Nevertheless, a reduction in cathodic current density is seen even after short immersion times of 0.5 h and is attributed to physical barrier layer formed locally over the cathodic sites. A greater reduction in cathodic current density is observed when coarse microstructure is conversion coating solution treated compared to conversion

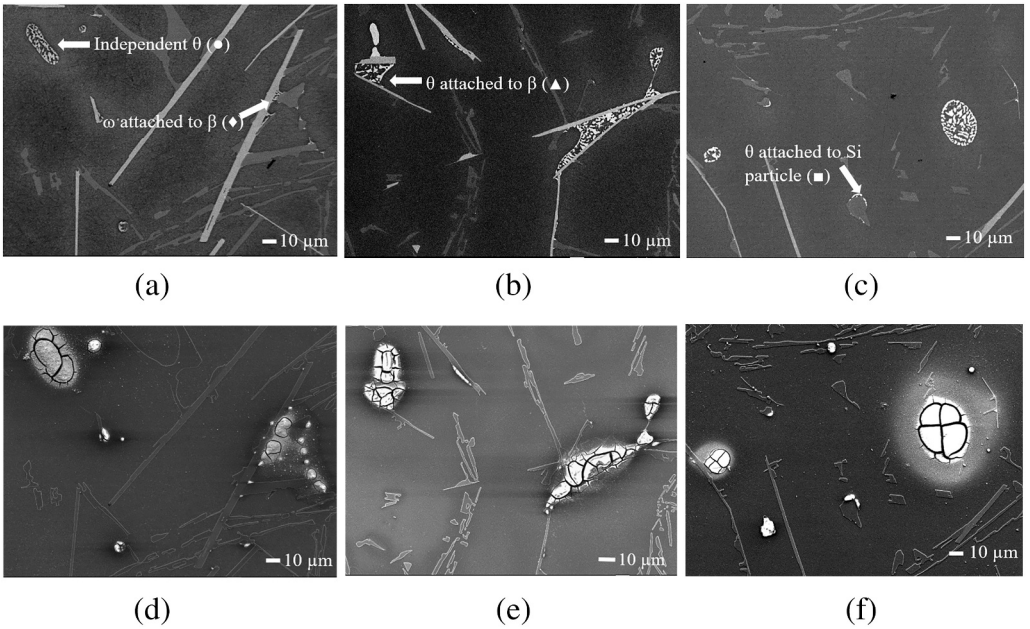

Fig. 4. (a), (b) and (c) coarse microstructures of slow solidified Al-7Si-2Cu-1Fe and corresponding local precipitate type deposit morphology after immersion for (d) 0.5 h, (e) 1 h and (f) 2 h characterised using SEM in secondary electron imaging mode.

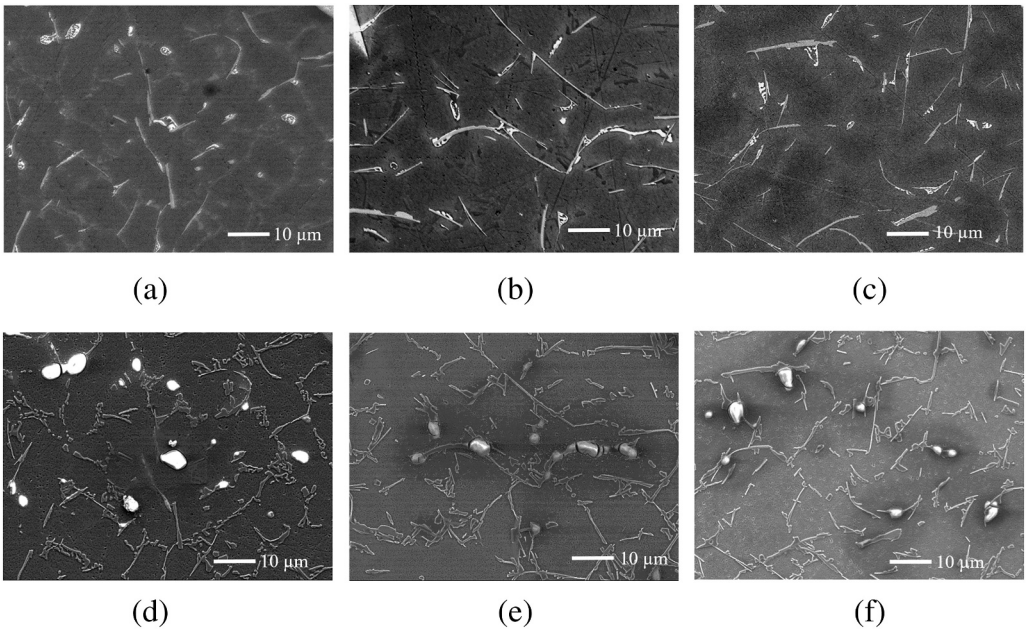

Fig. 5. (a), (b), and (c) fine microstructures of fast solidified Al-7Si-2Cu-1Fe and corresponding local precipitate type deposit morphology after immersion for (d) 0.5 h, (e) 1 h and (f) 2 h characterised using SEM using secondary electron imaging mode.

coating solution treated fine microstructures. It can be due to a greater number of cathodic sites being covered after immersion of coarse microstructure alloy in conversion coating solution (Table 3).

4. Conclusions

Cathodic IM particles play a crucial role in the deposition of CeCC on aluminium alloy substrates due to their effect on the local pH rise that triggers local conversion compound deposition. In this work, the influence the cathodic intermetallics' geometries and spatial distribution on the deposit initiation were studied. Microstructures of controlled cathodic feature size and spacing were synthesised for such an investigation. They were then immersed in a conversion coatings solution (0.1 M $Ce(NO_3)_3$ + 0.1 M NaCl) for short times (0.5 h, 1 h and 2 h) to observe local precipitate initiation and growth sequence. The deposition reaction was observed and quantified on a wide variety of IM, from which we can conclude that:

- Preferential heavy deposition occurs only on very active Cu-rich IM even at short immersion time of 0.5 h. A thin conversion coating layer may have formed on the rest of the surface and passivated the weakly cathodic Fe-rich IM, leading to no SEM discernible deposit even after long 18 h immersion.
- Cu-rich IM existing alone in the aluminium matrix showed different deposit lateral growth compared to Cu-containing IM in electrical contact with other second phases like Fe-containing β IM and Si particles. When existing alone, the deposit spread equally in all direction along the Cu-containing IM/Al matrix interface. When existing in contact with β IM or Si particles, the coating deposit spread laterally to a lesser extent across the Cu-rich IM/β IM interface and Cu-rich IM/Si particle interface as compared to lateral spread across the Cu-rich/Al matrix interface.

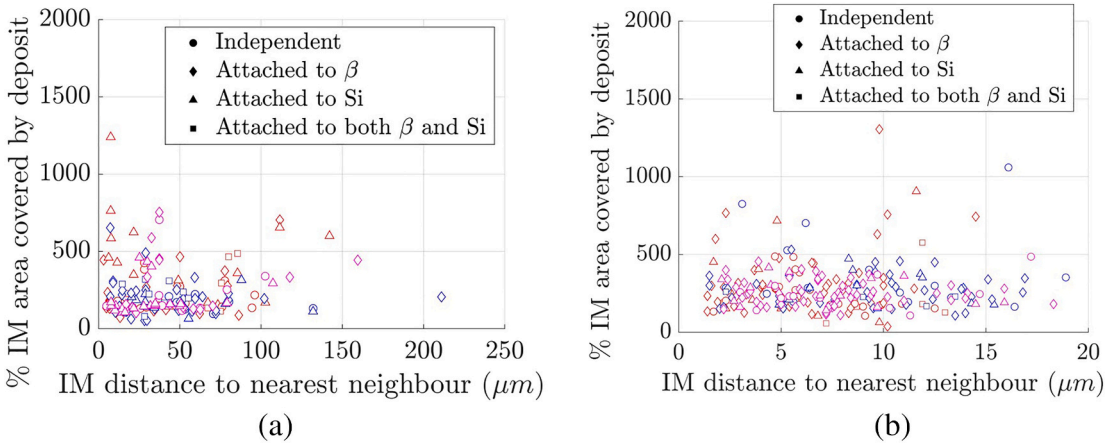

Fig. 6. Influence of nearest neighbour on deposition area extension over an IM observed in (a) slow solidified alloy (b) fast solidified alloy for different immersion times 0.5 h (red), 1 h (blue) and 2 h (magenta). (For interpretation of the references to colour in this figure legend, the reader is referred to the web version of this article.)

Table 3
Localised deposition numbers of the entire population of Cu-rich IM investigated in this study.

Microstructure	Immersion time	Total number of Cu-rich IM investigated	% number of IM covered with conversion compounds	Area fraction of bare Cu-rich IM	Area fraction of deposits over Cu-rich IM	Factor
Coarse	0.5 h	76	90.8	0.035	0.080	2.27
	1 h	66	92.4	0.036	0.066	1.85
	2 h	52	100.0	0.022	0.049	2.18
Fine	0.5 h	144	63.2	0.008	0.019	2.23
	1 h	88	81.8	0.008	0.022	2.62
	2 h	104	86.5	0.007	0.016	2.32

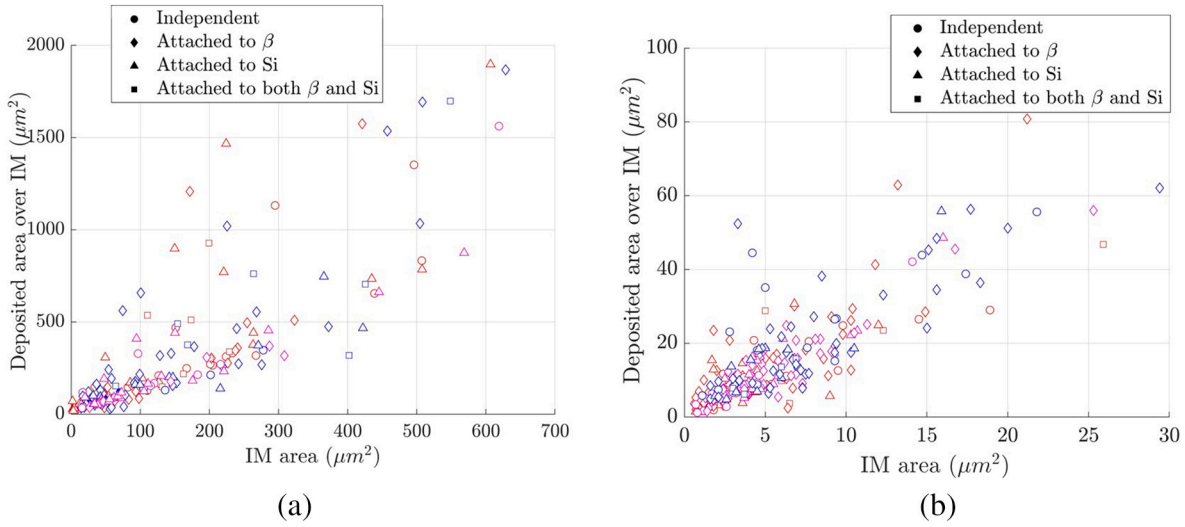

Fig. 7. Scatter plot showing the measured IM area before (x-axis) and after deposition (y-axis) for different immersion times 0.5 h (red), 1 h (blue) and 2 h (magenta) in alloy Al-7Si-2Cu-1Fe with (a) coarse and (b) fine microstructure. (For interpretation of the references to colour in this figure legend, the reader is referred to the web version of this article.)

Table 4
Correlation parameters obtained from linear correlation of data points reported in Fig. 7.

Microstructure	Immersion time	Slope of linear correlation line	Correlation coefficient (R^2)
Coarse	0.5 h	2.53	0.59
	1 h	1.96	0.88
	2 h	2.23	0.72
Fine	0.5 h	2.40	0.62
	1 h	2.60	0.71
	2 h	2.38	0.85

- Increased number of Cu-rich IMs activated for a deposition reaction when immersion time was increased from 0.5 h to 2 h.
- Big Cu-rich IM in the coarse microstructure activated faster than small Cu-rich IM in the fine microstructure. 100% of the big Cu-rich IM in coarse microstructure investigated in the study showed deposition after 2 h compared to 86% small Cu-rich IM in the fine microstructure.
- The size of the Cu-rich IM (surface area) correlated linearly with the amount of deposition on it in terms of lateral spread in x- and y-direction as well as outward in the z-direction.
- The slope of the linear correlation between deposit surface area and surface area of the underlying IM were similar for all immersion times, reported between 1.96 and 2.60, indicates that spontaneous deposition occurring after short 0.5 h immersion did significantly grow laterally for up to at least 2 h.
- The distance between two Cu-rich IM did not affect the extent of deposition over it. The pH gradient in the vicinity of the IM responsible for deposition reaction to occur is highly localised.

The approach to investigating the role of microstructure on conversion coating formation by controlling the cathodic IM geometry and spacing is novel. Therefore, more parameters should be investigated and compared. For example, different IM with varying cathodic potential can be considered. Longer time should also be monitored to verify the growth of the protective film further.

CRediT authorship contribution statement

1. Salil Sainis
   Contributed to the conception and design of the study, performed all the sample preparation, characterisation and image analyses as well as analysis and interpretation of data. The main contributor in writing and critical revision of the paper.
2. Sabrina Rosoiou
   Contributed to performing XRD experiments.

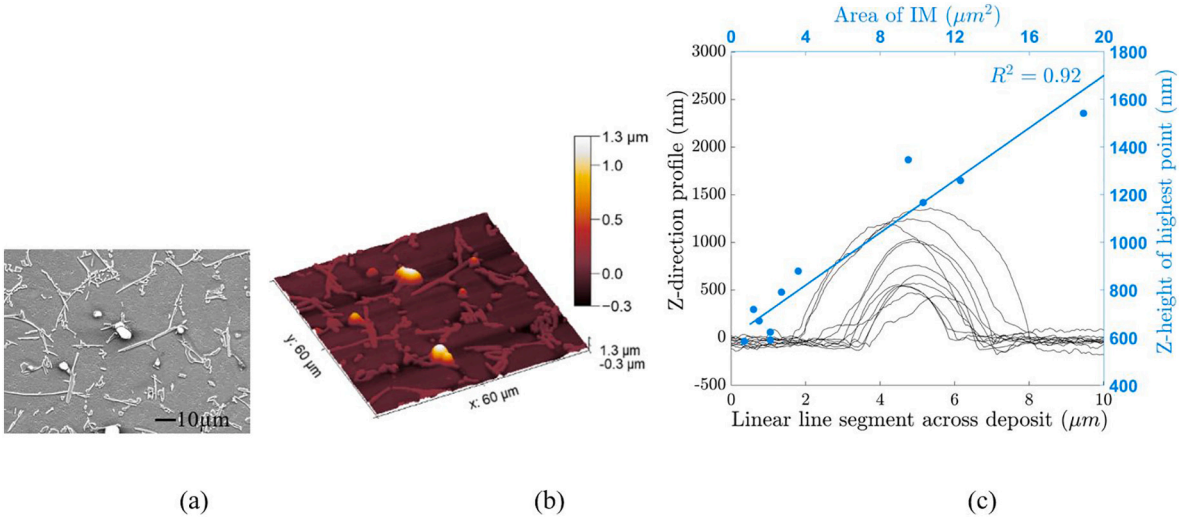

Fig. 8. (a) Morphology of a deposit region (after 2 h immersion) in a fast solidified alloy microstructure as observed with SEM in secondary electron imaging mode (b) topography of the same deposit region and (c) (i) primary y-axes: 2-D topography of deposit along the cross-sectional plane (linear line segment denoted in x-axis) where deposit reaction was seen to be the highest (ii) Secondary y-axis: the highest z-height of deposit and the area of IM.

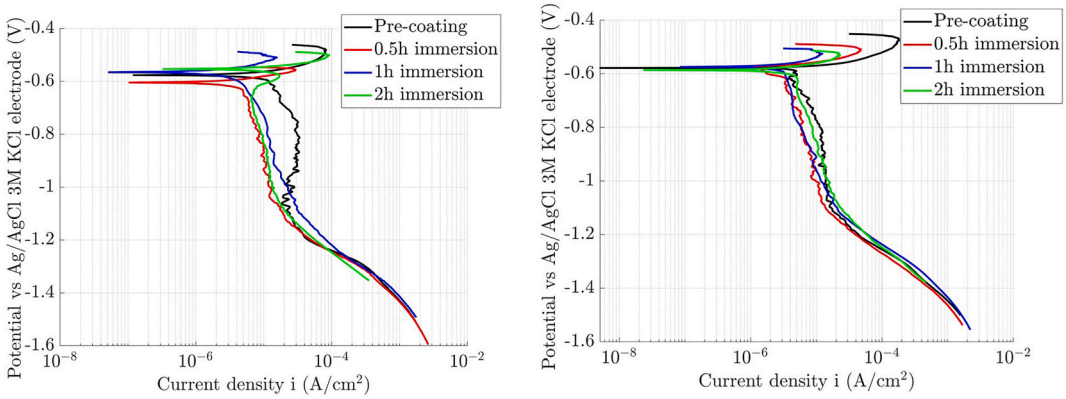

Fig. 9. Potentiodynamic polarization curves in 0.05 M NaCl solution for samples with (a) coarse microstructure (b) fine microstructure after subjecting to immersion coating treatment for different times.

Table 5
Electrochemical parameters obtained from cathodic polarization curves in Fig. 9.

Treatment	Coarse microstructure		Fine microstructure	
	E_{corr} (mV)	$i_{c,avg.}$ (μA/cm^2)	E_{corr} (mV)	$i_{c,avg.}$ (μA/cm^2)
Pre-coated	−589 ± 32	28.7 ± 5.0	−589 ± 24	11.5 ± 1.9
0.5 h immersion	−601 ± 6	9.2 ± 1.8	−589 ± 11	5.9 ± 2.3
1 h immersion	−586 ± 2	13.6 ± 3.3	−585 ± 7	7.3 ± 2.3
2 h immersion	−584 ± 3	10.0 ± 1.8	−590 ± 20	10.05 ± 2.69

3. Ehsan Ghassmali
   Contributed to setting up system and essential parameters for performing SEM characterisations, conception and design of alloy used in the study, analysis and interpretation of microstructure characterisation and involved in critical revision of the paper.
4. Caterina Zanella
   Contributed to the conception and design of the study, SKPFM experiments, analysis and interpretation of data. A major contributor to manuscript preparation and revision.

Declaration of competing interest

The authors declare that they have no known competing financial interests or personal relationships that could have appeared to influence the work reported in this paper.

Acknowledgement

The authors sincerely acknowledge the funding received from the European Union's Horizon 2020 - Research and Innovation Framework Programme under the H2020 Marie Skłodowska-Curie Actions grant agreement No 764977. The authors also acknowledge Centre for Surface Science and Nanotechnology at University Politehnica of Bucharest for XRD facilities.

References

[1] R.G. Buchheit, A compilation of corrosion potentials reported for intermetallic phases in aluminum alloys, J. Electrochem. Soc. 142 (1995) 3994, https://doi.org/10.1149/1.2048447.

[2] P. Schmutz, Characterisation of AA2024-T3 by scanning kelvin probe force microscopy, J. Electrochem. Soc. 145 (1998) 2285, https://doi.org/10.1149/1.1838633.

[3] N. Birbilis, R.G. Buchheit, Investigation and discussion of characteristics for intermetallic phases common to aluminum alloys as a function of solution pH, J. Electrochem. Soc. 155 (2008), https://doi.org/10.1149/1.2829897.

[4] N. Birbilis, R.G. Buchheit, Electrochemical characteristics of intermetallic phases in aluminum alloys: an experimental survey and discussion, J. Electrochem. Soc. 152 (2005), https://doi.org/10.1149/1.1869984.

[5] F. Andreatta, M.M. Lohrengel, H. Terryn, J.H.W. De Wit, Electrochemical characterisation of aluminium AA7075-T6 and solution heat treated AA7075 using a micro-capillary cell, Electrochim. Acta 48 (2003) 3239–3247, https://doi.org/10.1016/S0013-4686(03)00379-7.

[6] M. Gao, C.R. Feng, R.P. Wei, An analytical electron microscopy study of constituent particles in commercial 7075-T6 and 2024-T3 alloys, Metall. Mater. Trans. A Phys. Metall. Mater. Sci. 29 (1998) 1145–1151, https://doi.org/10.1007/s11661-998-0240-9.

[7] P. Schmutz, Corrosion study of AA2024-T3 by scanning kelvin probe force microscopy and in situ atomic force microscopy scratching, J. Electrochem. Soc. 145 (1998) 2295, https://doi.org/10.1149/1.1838634.

[8] R.L. Twite, G.P. Bierwagen, Review of alternatives to chromate for corrosion protection of aluminum aerospace alloys, Prog. Org. Coatings. 33 (1998) 91–100, https://doi.org/10.1016/S0300-9440(98)00015-0.

[9] T.G. Harvey, Cerium-based conversion coatings on aluminium alloys: a process review, Corros. Eng. Sci. Technol. 48 (2013) 248–269, https://doi.org/10.1179/1743278213Y.0000000089.

[10] D.B. Mitton, A. Carangelo, A. Acquesta, T. Monetta, M. Curioni, F. Bellucci, Selected Cr(VI) replacement options for aluminum alloys: a literature survey, Corros. Rev. 35 (2017) 365–381, https://doi.org/10.1515/corrrev-2016-0059.

[11] I. Milošev, G.S. Frankel, Review—conversion coatings based on zirconium and/or titanium, J. Electrochem. Soc. 165 (2018) C127–C144, https://doi.org/10.1149/2.0371803jes.

[12] J.. Nordlien, J.. Walmsley, H. Østerberg, K. Nisancioglu, Formation of a zirconium-titanium based conversion layer on AA 6060 aluminium, Surf. Coatings Technol. 153 (2002) 72–78, https://doi.org/10.1016/S0257-8972(01)01663-2.

[13] O. Lunder, C. Simensen, Y. Yu, K. Nisancioglu, Formation and characterisation of Ti–Zr based conversion layers on AA6060 aluminium, Surf. Coatings Technol. 184 (2004) 278–290, https://doi.org/10.1016/J.SURFCOAT.2003.11.003.

[14] X. Zuo, W. Li, S. Mu, J. Du, Y. Yang, P. Tang, Investigation of composition and structure for a novel Ti–Zr chemical conversion coating on 6063 aluminum alloy, Prog. Org. Coatings. 87 (2015) 61–68, https://doi.org/10.1016/J.PORGCOAT.2015.05.008.

[15] L. Li, B.W. Whitman, G.M. Swain, Characterisation and performance of a Zr/Ti pretreatment conversion coating on AA2024-T3, J. Electrochem. Soc. 162 (2015) C279–C284, https://doi.org/10.1149/2.0901506jes.

[16] A.. Davenport, H.. Isaacs, M.. Kendig, XANES investigation of the role of cerium compounds as corrosion inhibitors for aluminum, Corros. Sci. 32 (1991) 653–663, https://doi.org/10.1016/0010-938X(91)90113-4.

[17] L. Paussa, F. Andreatta, N.C. Rosero Navarro, A. Durán, L. Fedrizzi, Study of the effect of cerium nitrate on AA2024-T3 by means of electrochemical micro-cell technique, Electrochim. Acta 70 (2012) 25–33, https://doi.org/10.1016/J.ELECTACTA.2012.02.099.

[18] A.E. Hughes, J.D. Gorman, P.R. Miller, B.A. Sexton, P.J.K. Paterson, R.J. Taylor, Development of cerium-based conversion coatings on 2024-T3 Al alloy after rare-earth desmutting, Surf. Interface Anal. 36 (2004) 290–303, https://doi.org/10.1002/sia.1652.

[19] B.R.W. Hinton, D.R. Arnott, N.E. Ryan, Cerium conversion coatings for the corrosion protection of aluminium, Mater. Forum. 9 (1986) 162–173.

[20] A.E. Hughes, R.J. Taylor, B.R.W. Hinton, L. Wilson, XPS and SEM characterisation of hydrated cerium oxide conversion coatings, Surf. Interface Anal. 23 (1995) 540–550, https://doi.org/10.1002/sia.740230714.

[21] A.J. Aldykewicz Jr., H.S. Isaacs, A.J. Davenport, The investigation of cerium as a cathodic inhibitor for aluminium-copper alloys, J. Electrochem. Soc. 142 (1995) 3342–3351 http://jes.ecsdl.org/content/142/10/3342.full.pdf+html.

[22] A.E. Hughes, J.D. Gorman, P.J.K. Paterson, The characterisation of Ce-Mo-based conversion coatings on Al-alloys: part I, Corros. Sci. 38 (1996) 1957–1976, https://doi.org/10.1016/S0010-938X(96)00088-1.

[23] M. Dabalà, L. Armelao, A. Buchberger, I. Calliari, Cerium-based conversion layers on aluminum alloys, Appl. Surf. Sci. 172 (2001) 312–322, https://doi.org/10.1016/S0169-4332(00)00873-4.

[24] M.A. Arenas, M. Bethencourt, F.J. Botana, J. de Damborenea, M. Marcos, Inhibition of 5083 aluminium alloy and galvanised steel by lanthanide salts, Corros. Sci. 43 (2001) 157–170, https://doi.org/10.1016/S0010-938X(00)00051-2.

[25] A. Aballe, M. Bethencourt, F.J. Botana, M.J. Cano, M. Marcos, On the mixed nature of cerium conversion coatings, Mater. Corros. 53 (2002) 176–184, https://doi.org/10.1002/1521-4176(200203)53:3<176::AID-MACO176>3.0.CO;2-K.

[26] A. Kolics, A.S. Besing, P. Baradlai, A. Wieckowski, Cerium deposition on aluminum alloy 2024-T3 in acidic NaCl solutions, J. Electrochem. Soc. 150 (2003) B512, https://doi.org/10.1149/1.1615995.

[27] P. Campestrini, H. Terryn, A. Hovestad, J.H.. de Wit, Formation of a cerium-based conversion coating on AA2024: relationship with the microstructure, Surf. Coatings Technol. 176 (2004) 365–381, https://doi.org/10.1016/S0257-8972(03)00743-6.

[28] B. Davó, J.J. de Damborenea, Use of rare earth salts as electrochemical corrosion inhibitors for an Al–Li–Cu (8090) alloy in 3.56% NaCl, Electrochim. Acta 49 (2004) 4957–4965, https://doi.org/10.1016/J.ELECTACTA.2004.06.008.

[29] I. Danaee, H.R. Zamanizadeh, M. Fallahi, B. Lotfi, The effect of surface pre-treatments on corrosion behavior of cerium-based conversion coatings on Al 7075-T6, Mater. Corros. 65 (2014) 815–819, https://doi.org/10.1002/maco.201307147.

[30] L. Paussa, F. Andreatta, D. De Felicis, E. Bemporad, L. Fedrizzi, Investigation of AA2024-T3 surfaces modified by cerium compounds: a localised approach, Corros. Sci. 78 (2014) 215–222, https://doi.org/10.1016/J.CORSCI.2013.10.001.

[31] M. Eslami, M. Fedel, G. Speranza, F. Deflorian, N.-E. Andersson, C. Zanella, Study of selective deposition mechanism of cerium-based conversion coating on Rheo-HPDC aluminium-silicon alloys, Electrochim. Acta 255 (2017) 449–462, https://doi.org/10.1016/J.ELECTACTA.2017.09.182.

[32] M. Eslami, M. Fedel, G. Speranza, F. Deflorian, C. Zanella, Deposition and characterisation of cerium-based conversion coating on HPDC low Si content aluminum alloy, J. Electrochem. Soc. 164 (2017) C581–C590, https://doi.org/10.1149/2.1511709jes.

[33] G. Šekularac, I. Milošev, Electrochemical behavior and self-sealing ability of zirconium conversion coating applied on aluminum alloy 3005 in 0.5 M NaCl solution, J. Electrochem. Soc. 167 (2020) 021509, , https://doi.org/10.1149/1945-7111/ab6b0d.

[34] M. Becker, Chromate-free chemical conversion coatings for aluminum alloys in: Corrosion Reviews Volume 37 Issue 4 (2019), Corros. Rev. 37 (2019) 321–342 https://www.degruyter.com/view/journals/corrrev/37/4/article-p321.xml , Accessed date: 4 June 2020.

[35] C.A. Munson, G.M. Swain, Structure and chemical composition of different variants of a commercial trivalent chromium process (TCP) coating on aluminum alloy 7075-T6, Surf. Coatings Technol. 315 (2017) 150–162, https://doi.org/10.1016/J.SURFCOAT.2017.02.018.

[36] W. Zhan, X. Liu, G. OuYang, Film-forming mechanism and properties of Ti/Zr/Mo colored conversion coating prepared on aluminum alloy, Int. J. Precis. Eng. Manuf. Technol. 3 (2016) 297–302, https://doi.org/10.1007/s40684-016-0038-y.

[37] J. Cerezo, I. Vandendael, R. Posner, J.H.W. De Wit, J.M.C. Mol, H. Terryn, The effect of surface pre-conditioning treatments on the local composition of Zr-based conversion coatings formed on aluminium alloys, Appl. Surf. Sci. 366 (2016) 339–347, https://doi.org/10.1016/j.apsusc.2016.01.106.

[38] J. Cerezo, I. Vandendael, R. Posner, K. Lill, J.H.W. de Wit, J.M.C. Mol, H. Terryn, Initiation and growth of modified Zr-based conversion coatings on multi-metal surfaces, Surf. Coatings Technol. 236 (2013) 284–289, https://doi.org/10.1016/j.surfcoat.2013.09.059.

[39] D. Peng, J. Wu, X. Yan, X. Du, Y. Yan, X. Li, The formation and corrosion behavior of a zirconium-based conversion coating on the aluminum alloy AA6061, J. Coatings Technol. Res. 13 (2016) 837–850, https://doi.org/10.1007/s11998-016-9789-1.

[40] A. Sarfraz, R. Posner, M.M. Lange, K. Lill, A. Erbe, Role of intermetallics and copper in the deposition of ZrO 2 conversion coatings on AA6014, J. Electrochem. Soc. 161 (2014) C509–C516, https://doi.org/10.1149/2.0121412jes.

[41] F.O. George, P. Skeldon, G.E. Thompson, Formation of zirconium-based conversion coatings on aluminium and Al-Cu alloys, Corros. Sci. 65 (2012) 231–237, https://doi.org/10.1016/j.corsci.2012.08.031.

[42] X. Verdalet-Guardiola, B. Fori, J.P. Bonino, S. Duluard, C. Blanc, Nucleation and growth mechanisms of trivalent chromium conversion coatings on 2024-T3 aluminium alloy, Corros. Sci. 155 (2019) 109–120, https://doi.org/10.1016/j.corsci.2019.04.035.

[43] C.F. Glover, M.L.C. Lim, G. Post, M. Mayo, J.R. Scully, The effect of surface treatment on the performance of a trivalent chromium process (TCP) pretreatment on AA7075 aerospace alloys for the protection against filiform corrosion, Corrosion 75 (2019) 1513–1526, https://doi.org/10.5006/3380.

[44] T.K. Shruthi, G.M. Swain, Communication—role of trivalent chromium on the anti-corrosion properties of a TCP conversion coating on aluminum alloy 2024-T3, J. Electrochem. Soc. 165 (2018) C103–C105, https://doi.org/10.1149/2.1301802jes.

[45] R. Saillard, B. Viguier, G. Odemer, A. Pugliara, B. Fori, C. Blanc, Influence of the microstructure on the corrosion behaviour of 2024 aluminium alloy coated with a trivalent chromium conversion layer, Corros. Sci. (2018), https://doi.org/10.1016/J.CORSCI.2018.07.007.

[46] J. Qi, T. Hashimoto, J. Walton, X. Zhou, P. Skeldon, G.E. Thompson, Formation of a trivalent chromium conversion coating on AA2024-T351 alloy, J. Electrochem. Soc. 163 (2016) C25–C35, https://doi.org/10.1149/2.0771602jes.

[47] D.R. Arnott, N.E. Ryan, B.R.W. Hinton, B.A. Sexton, A.E. Hughes, Auger and XPS studies of cerium corrosion inhibition on 7075 aluminum alloy, Appl. Surf. Sci. 22–23 (1985) 236–251, https://doi.org/10.1016/0378-5963(85)90056-X.

[48] B.L. Treu, S. Joshi, W.R. Pinc, M. O'Keefe, W. Fahrenholtz, Sub-surface electrochemical effects on the spontaneous deposition of cerium conversion coatings on aluminum alloys, ECS Trans, The Electrochemical Society, 2009, pp. 101–113, , https://doi.org/10.1149/1.3259802.

[49] B. Davó, A. Conde, J.J. De Damborenea, Inhibition of stress corrosion cracking of alloy AA8090 T-8171 by addition of rare earth salts, Corros. Sci. 47 (2005) 1227–1237, https://doi.org/10.1016/j.corsci.2004.07.028.

[50] B.L. Treu, S. Joshi, W.R. Pinc, M.J. O'Keefe, W.G. Fahrenholtz, Characterisation of localized surface states of Al 7075-T6 during deposition of cerium-based conversion coatings, J. Electrochem. Soc. 157 (2010) C282, https://doi.org/10.1149/1.3454236.

[51] W.G. Fahrenholtz, M.J. O'Keefe, H. Zhou, J.T. Grant, Characterisation of cerium-based conversion coatings for corrosion protection of aluminum alloys, Surf.

Coatings Technol. 155 (2002) 208–213, https://doi.org/10.1016/S0257-8972(02)00062-2.
[52] B.Y. Johnson, J. Edington, M.J. O'Keefe, Effect of coating parameters on the microstructure of cerium oxide conversion coatings, Mater. Sci. Eng. A 361 (2003) 225–231, https://doi.org/10.1016/S0921-5093(03)00516-1.
[53] B.F. Rivera, B.Y. Johnson, M.J. O'Keefe, W.G. Fahrenholtz, Deposition and characterisation of cerium oxide conversion coatings on aluminum alloy 7075-T6, Surf. Coatings Technol. 176 (2004) 349–356, https://doi.org/10.1016/S0257-8972(03)00742-4.
[54] J.H. Xu, X. Wang, J. Wang, Q.J. Zheng, Study on technological process of cerium-based conversion coating on aluminum, Adv. Mater. Res. 79–82 (2009) 879–882, https://doi.org/10.4028/www.scientific.net/AMR.79-82.879.
[55] D. Lau, A.M. Glenn, A.E. Hughes, F.H. Scholes, T.H. Muster, S.G. Hardin, Factors influencing the deposition of Ce-based conversion coatings, part II: the role of localised reactions, Surf. Coatings Technol. 203 (2009) 2937–2945, https://doi.org/10.1016/J.SURFCOAT.2009.03.016.
[56] W. Pinc, S. Maddela, M. O'Keefe, W. Fahrenholtz, Formation of subsurface crevices in aluminum alloy 2024-T3 during deposition of cerium-based conversion coatings, Surf. Coatings Technol. 204 (2010) 4095–4100, https://doi.org/10.1016/J.SURFCOAT.2010.05.039.
[57] A. Decroly, J.-P. Petitjean, Study of the deposition of cerium oxide by conversion on to aluminium alloys, Surf. Coatings Technol. 194 (2005) 1–9, https://doi.org/10.1016/J.SURFCOAT.2004.05.012.
[58] B. Valdez, S. Kiyota, M. Stoytcheva, R. Zlatev, J.M. Bastidas, Cerium-based conversion coatings to improve the corrosion resistance of aluminium alloy 6061-T6, Corros. Sci. 87 (2014) 141–149, https://doi.org/10.1016/J.CORSCI.2014.06.023.
[59] F.H. Scholes, C. Soste, A.E. Hughes, S.G. Hardin, P.R. Curtis, The role of hydrogen peroxide in the deposition of cerium-based conversion coatings, Appl. Surf. Sci. 253 (2006) 1770–1780, https://doi.org/10.1016/J.APSUSC.2006.03.010.
[60] D.C. Chen, G.X. Wu, W.F. Li, W.H. Gong, Y.Q. Liang, Preparing an environment-benignly rare-earth based chemical conversion coatings on 6063 aluminium alloy, Key Eng. Mater. 373–374 (2008) 224–227, https://doi.org/10.4028/www.scientific.net/KEM.373-374.224.
[61] R.U. Din, N. Tabrizian, M.S. Jellesen, R. Ambat, Aluminium alloy AA6060 surface treatment with high temperature steam containing chemical additives, Mater. Today Proc. 2 (2015) 5063–5070, https://doi.org/10.1016/J.MATPR.2015.10.097.
[62] D.C. Chen, W.F. Li, W.H. Gong, G.X. Wu, J.F. Wu, Microstructure and formation mechanism of Ce-based chemical conversion coating on 6063 Al alloy, 19 (3) (2009) 592–600, https://doi.org/10.1016/S1003-6326(08)60318-0.
[63] K.A. Yasakau, M.L. Zheludkevich, S.V. Lamaka, M.G.S. Ferreira, Mechanism of corrosion inhibition of AA2024 by rare-earth compounds, J. Phys. Chem. B 110 (2006) 5515–5528, https://doi.org/10.1021/jp0560664.
[64] A. Pardo, M.C. Merino, R. Arrabal, F. Viejo, M. Carboneras, Improvement of corrosion behavior of A3xx.x/SiCp composites in 3.5 wt % NaCl solution by Ce surface coatings, J. Electrochem. Soc. 153 (2006) B52, https://doi.org/10.1149/1.2150151.
[65] C.A. Schneider, W.S. Rasband, K.W. Eliceiri, NIH Image to ImageJ: 25 years of image analysis, Nat. Methods 9 (2012) 671–675, https://doi.org/10.1038/nmeth.2089.
[66] E. Sjölander, Heat Treatment of Al-Si-Cu-Mg Casting Alloys, School of Engineering, Jönköping University, 2011.
[67] Y.H. Cho, H.C. Lee, K.H. Oh, A.K. Dahle, Effect of strontium and phosphorus on eutectic Al-Si nucleation and formation of β-Al5FeSi in hypoeutectic Al-Si foundry alloys, Metall. Mater. Trans. A Phys. Metall. Mater. Sci. 39 (2008) 2435–2448, https://doi.org/10.1007/s11661-008-9580-8.
[68] W. Zhang, B. Lin, Z. Luo, Y. Zhao, Y. Li, Formation of Fe-rich intermetallic compounds and their effect on the tensile properties of squeeze-cast Al–Cu alloys, J. Mater. Res. 30 (2015) 2474–2484, https://doi.org/10.1557/jmr.2015.215.
[69] E. Samuel, A.M. Samuel, H.W. Doty, S. Valtierra, F.H. Samuel, Intermetallic phases in Al–Si based cast alloys: new perspective, Int. J. Cast Met. Res. 27 (2014) 107–114, https://doi.org/10.1179/1743133613Y.0000000083.
[70] M.V. Kral, H.R. McIntyre, M.J. Smillie, Identification of intermetallic phases in a eutectic Al-Si casting alloy using electron backscatter diffraction pattern analysis, Scr. Mater. 51 (2004) 215–219, https://doi.org/10.1016/j.scriptamat.2004.04.015.
[71] PDF-00-004-0787, PDF-00-004-0787, (1953).
[72] PDF-00-027-1402, No title, Natl. Bur. Stand. (United States), Natl. Bur. Stand. Monogr. (35) (1976) 2513.
[73] P. Tang, W. Li, K. Wang, J. Du, X. Chen, Y. Zhao, W. Li, Effect of Al-Ti-C master alloy addition on microstructures and mechanical properties of cast eutectic Al-Si-Fe-Cu alloy, Mater. Des. 115 (2017) 147–157, https://doi.org/10.1016/J.MATDES.2016.11.036.
[74] T. Tunçay, S. Bayoğlu, The effect of iron content on microstructure and mechanical properties of A356 cast alloy, Metall. Mater. Trans. B Process Metall. Mater. Process. Sci. 48 (2017) 794–804, https://doi.org/10.1007/s11663-016-0909-1.
[75] S. Beroual, Z. Boumerzoug, P. Paillard, Y. Borjon-Piron, Effects of heat treatment and addition of small amounts of Cu and Mg on the microstructure and mechanical properties of Al-Si-Cu and Al-Si-Mg cast alloys, J. Alloys Compd. 784 (2019) 1026–1035, https://doi.org/10.1016/J.JALLCOM.2018.12.365.
[76] M.L. Öveçoğlu, N. Ünlü, N. Eruslu, A. Genç, Characterisation investigations of a melt-spun ternary Al–8Si–5.1Cu (in wt.%) alloy, Mater. Lett. 57 (2003) 3296–3301, https://doi.org/10.1016/S0167-577X(03)00051-X.
[77] B. Göğebakan, O. Avar, Uzun, Quasicrystalline phase formation in the conventionally solidified Al–Cu–Fe system, Mater. Sci. 27 (2009) 919–926.
[78] A. Školáková, P. Novák, L. Mejzlíková, F. Průša, P. Salvetr, D. Vojtěch, Structure and mechanical properties of Al-Cu-Fe-X alloys with excellent thermal stability, Materials (Basel) 10 (2017) 1269, https://doi.org/10.3390/ma10111269.
[79] J. Hu, X.H. Zhao, S.W. Tang, M.R. Sun, Corrosion protection of aluminum borate whisker reinforced AA6061 composite by cerium oxide-based conversion coating, Surf. Coatings Technol. 201 (2006) 3814–3818, https://doi.org/10.1016/J.SURFCOAT.2006.09.006.
[80] I. Milošev, B. Volarič, Conversion coatings based on rare earth nitrates and chlorides for corrosion protection of aluminum alloy 7075-T6, CORROSION 73 (2017) 822–843, https://doi.org/10.5006/2353.
[81] L.G. Bland, N. Birbilis, J.R. Scully, Exploring the effects of intermetallic particle size and spacing on the corrosion of Mg-Al alloys using model electrodes, J. Electrochem. Soc. 163 (2016) C895–C906, https://doi.org/10.1149/2.1151614jes.
[82] H. Pan, K. Pang, F. Cui, F. Ge, C. Man, X. Wang, Z. Cui, Effect of alloyed Sr on the microstructure and corrosion behavior of biodegradable Mg-Zn-Mn alloy in Hanks' solution, Corros. Sci. 157 (2019) 420–437, https://doi.org/10.1016/j.corsci.2019.06.022.